Wang, Youjiang; Mikkola, Tommi; Hirdaris, Spyros

A fast and storage-saving method for direct volumetric integration of FWH acoustic analogy

Published in:
Ocean Engineering

DOI:
10.1016/j.oceaneng.2022.112087

Published: 01/10/2022

Document Version
Publisher's PDF, also known as Version of record

Please cite the original version:
Wang, Y., Mikkola, T., & Hirdaris, S. (2022). A fast and storage-saving method for direct volumetric integration of FWH acoustic analogy. *Ocean Engineering*, *261*, Article 112087.
https://doi.org/10.1016/j.oceaneng.2022.112087

Ocean Engineering 261 (2022) 112087

Contents lists available at ScienceDirect

Ocean Engineering

journal homepage: www.elsevier.com/locate/oceaneng

A fast and storage-saving method for direct volumetric integration of FWH acoustic analogy

Youjiang Wang [a,b], Tommi Mikkola [c], Spyros Hirdaris [c,*]

[a] State Key Laboratory of Ocean Engineering, Shanghai Jiao Tong University, 200240 Shanghai, China
[b] School of Naval Architecture, Ocean & Civil Engineering, Shanghai Jiao Tong University, 200240 Shanghai, China
[c] School of engineering, Marine Technology Group, Aalto University, 00076, Espoo, Finland

ARTICLE INFO

Keywords:
Underwater noise
Acoustic analogy
Dual mesh technique
Cavitation
Propeller

ABSTRACT

This paper proposes a new method that makes the direct volume integration of the Lighthill stress term in FWH acoustic analogy affordable in terms of both computational time and disk storage requirement. The method is based on a dual mesh concept, i.e. while a fine mesh is used in CFD, a relatively coarse mesh is used for the acoustic calculation. The terms being independent of the observer positions in the integral formula of FWH acoustic analogy are calculated on the CFD mesh and mapped onto the acoustic mesh during the simulation. These sound source terms are used for the on-the-fly acoustic computation or saved for later use in the post-processing. A formulation of the Lighthill stress tensor in cavitating flow is also derived. The method is verified with the acoustic assessment of an inclined marine propeller case. A reduction of the calculation time by 98% and disk storage by 99% is achieved while maintaining small acoustic error.

1. Introduction

In today's environmentally conscious world maritime innovation is expected to reflect the increasing societal demands to minimize the impact of shipping on the environment (Hirdaris and Cheng, 2012). Accordingly, current and future ship designs are expected to comply against demanding environmental standards. It has been reported that the underwater background noise is raised by a significant value due to human activities including shipping (Krasilnikov, 2019). This background noise raising as well as the impulsing underwater noise can very probably cause damage to marine life (Schack et al., 2019; European-Commission, 2019). However, the underwater radiated noise (URN) regulations are still premature. Investigations on URN with direct application on ships and marine propellers would be beneficial for regulatory authorities and green ship designs.

Both experimental and numerical methods were developed for the prediction of hydroacoustic emissions. Validated numerical URN prediction methods are considered particularly beneficial as they may boost the design and optimization of noise mitigation measures. They could also help set up reliable experiments and understand scale-effects. A currently popular numerical method is to couple Computational Fluid Mechanics (CFD) with acoustic analogies. A widely adopted acoustic analogy is the Ffowcs Williams–Hawkings (FWH) analogy (Williams and Hawkings, 1969). VTT also adopted the Lighthill analogy for the model of propeller radiated noise in cavitation tunnels (Hynninen et al., 2017; Viitanen et al., 2017, 2018). Some differences exist among the methods using the FWH analogy. In such case it is important to distinct between two approaches namely "direct" and "permeable" (or porous) FWH formulation. The former is to calculate the contribution of Lighthill stress tensor directly with volumetric integration and other terms on the real solid surface (Cianferra, 2017; Ianniello et al., 2014). On the other hand, the permeable FWH approach uses a data surface named "permeable surface" that encompasses all main sound sources. In this way, theoretically, all noise effect inside this surface can be idealized by virtual sources on it (Di Francescantonio, 1997). The permeable FWH approach is preferred by most researchers, although it faces additional numerical difficulties and accuracy problems (Testa et al., 2021; Lidtke et al., 2019; Wang et al., 2020; Spalart et al., 2019). This is because the direct FWH approach is deemed unfeasible for engineering problems due to two aspects. The first aspect is the huge disk storage requirement to save the volumetric hydroacoustic data in each time step and computational cell. The other aspect is the large amount of calculation time to integrate over all computational cells for acoustic assessment.

Cianferra (2017) applied both the direct and permeable FWH formulations for the fluid dynamic noise prediction of a finite size square cylinder at Re = 4000. This work demonstrated that the permeable formulation may successfully predict the main frequency components. However, the pressure fluctuation amplitudes can be underestimated

* Corresponding author.
E-mail addresses: youjiang.wang@sjtu.edu.cn (Y. Wang), spyros.hirdaris@aalto.fi (S. Hirdaris).

https://doi.org/10.1016/j.oceaneng.2022.112087
Received 25 January 2022; Received in revised form 16 June 2022; Accepted 19 July 2022
Available online 4 August 2022

and the solutions can be sensitive to the position of permeable surface. On the contrary, the direct approach can provide a noise prediction very similar to the accurate reference data. Cianferra et al. (2019) compared the direct and permeable FWH formulations further in the case of an irrotational advected vortex. The analysis showed that the permeable formulation does suffer from the end cap problem, while the direct formulation does not.

Testa et al. (2021), Sezen et al. (2020, 2021), Lloyd et al. (2015), Lidtke et al. (2019), and Li et al. (2018) all adopted the permeable FWH approach in their simulations. However, Testa et al. (2021), Lloyd et al. (2015), and Lidtke et al. (2019) all pointed out that spurious noise can occur when vortices penetrate the permeable surface. Based on these observations, a cylinder with open-cap around the propeller is a widely adopted configuration. However, open-cap cannot solve the problems totally, especially for situations where the propeller works in real operation. In such cases, vortices would also penetrate the cylinder side surface. Besides, in cavitating situations, it is highly doubtful that the unclosed permeable surface could capture the cavitation volume variation correctly.

To improve the feasibility of direct FWH formulation, Gadalla et al. (2021) applied a data-driven dimensionality reduction algorithms to alleviate the disk storage requirement for storing the volumetric hydroacoustic data. The algorithms were based on Dynamic Mode Decomposition mid cast and Proper Orthogonal Decomposition with interpolation. Both models showed the ability to reconstruct the flow using half of the original Large Eddy Simulation (LES) dataset.

This paper proposes a model that will improve the feasibility of direct FWH formulation. A dual mesh technique is used to reduce both the acoustic calculation time and the disk storage requirement for storing transient sound source information. This technique can make the volumetric integration even less resource-consuming than the surface integration without sacrificing significant accuracy. Section 2 presents the theory and numerical implementation of the new method. The numerical results to verify its effect is given in Section 3 and conclusions are drawn in Section 4. The corresponding code of this work has been made open-access under https://gitlab.com/youjiang-wang/libacousticsplus.

2. Methodology

2.1. FWH acoustic analogy

The FWH acoustic analogy is a further development upon Lighthill analogy (Lighthill, 1954) and Curle analogy (Curle, 1955). They are all deduced from the Navier–Stokes equations and expressed as non-homogeneous wave equation about sound pressure p' or density perturbation ρ'. The specialty of FWH analogy is that surfaces with arbitrary motion and penetration velocity can be correctly modeled as sound sources.

The original FWH analogy given by Williams and Hawkings (1969) is as follows

$$\left(\frac{\partial^2}{\partial t^2}-c_0^2\frac{\partial^2}{\partial x_i^2}\right)\rho' = \frac{\partial}{\partial t}\left[\left(\rho(v_i-u_i)+\rho_0 v_i\right)\delta(f)\frac{\partial f}{\partial x_i}\right] - \frac{\partial}{\partial x_i}\left[\left(\rho v_i(v_j-u_j)+P_{ij}\right)\delta(f)\frac{\partial f}{\partial x_j}\right] + \frac{\partial^2}{\partial x_i \partial x_j}\left[T_{ij}H(f)\right] \tag{1}$$

where f is a continuous field function to define the sound source surfaces, i.e. $f<0$, $f=0$, and $f>0$ mean positions inside, on, and outside the surface, respectively; $\delta(\cdot)$ is the Dirac delta function, $H(\cdot)$ is the Heaviside function; c_0 is the sound speed; ρ is the local density; ρ' is density's deviation from the uniform reference state ρ_0, i.e. $\rho'=\rho-\rho_0$; t is time; x is spatial coordinate; v and u are surface motion velocity and flow velocity, respectively; P_{ij} and T_{ij} are the compressive and Lighthill stress tensors, respectively. It can be observed that the first two terms on the right hand side of Eq. (1) are surface terms, while the third term has a volumetric distribution.

Assuming incompressible flow, the compressive stress tensor becomes

$$P_{ij} = p\delta_{ij} - \tau_{ij} \tag{2}$$

where p is the local field pressure, τ_{ij} the viscous stress tensor, and δ_{ij} the identity tensor. When Reynolds Averaged Navier–Stokes(RANS) equation is used, the Reynolds Stress should be included in τ_{ij}. The effect of τ_{ij} is normally negligibly small in comparison to $p\delta_{ij}$.

The Lighthill stress tensor T_{ij} is defined as

$$T_{ij} = \rho u_i u_j - \tau_{ij} + (p' - c_0^2\rho')\delta_{ij} \tag{3}$$

where p' presents the deviation of pressure from the uniform reference state p_0, i.e. $p' = p-p_0$. The three terms on the right hand side of Eq. (3) represent the non-linear convective forces described by velocity stress tensor, the viscous forces, and the deviation from a uniform sound velocity or the deviation from the isentropic behavior, respectively. Normally, the third term $(p'-c_0^2\rho')$ is small for single component fluid, and is exactly zero if isentropic fluid and the linear constitutive relation $(\mathrm{d}p = c_0^2\mathrm{d}\rho)$ are assumed.

The above-mentioned third term could be large for multiphase flow. That is because the density fluctuation is then mainly caused by convection or phase change rather than compression. Using ρ_{mix} for ρ and $\rho_{l,0}$ for ρ_0 to emphasize that the local flow is multiphase and the reference state is single liquid phase, and using ρ_l for the liquid density under the local pressure, we have

$$p' - c_0^2\rho' = p' - c_0^2(\rho_{mix}-\rho_{l,0}) = p' - c_0^2(\rho_l-\rho_{l,0}) - c_0^2(\rho_{mix}-\rho_l) \tag{4}$$

For $\rho_l' = \rho_l - \rho_{l,0}$, the Lighthill stress tensor becomes

$$T_{ij} = \rho u_i u_j - \tau_{ij} + \left[(p'-c_0^2\rho_l') - c_0^2(\rho_{mix}-\rho_l)\right]\delta_{ij} \tag{5}$$

In Eq. (5) the term $(p'-c_0^2\rho_l')$ is still negligible. However, the term $c_0^2(\rho_{mix}-\rho_l)$ could be large as the involvement of other phases could make ρ_{mix} far from ρ_l.

$$\rho_{mix} = \alpha_l\rho_l + (1-\alpha_l)\rho_v$$

$$T_{ij} = \rho u_i u_j - \tau_{ij} + (p'-c_0^2\rho_l')\delta_{ij} + c_0^2(1-\alpha_l)(\rho_l-\rho_v)\delta_{ij}$$

When the volume of fluid approach is used to idealize two phase cavitating flow in the CFD simulation, the Lighthill stress tensor can be written as

$$T_{ij} = \rho u_i u_j - \tau_{ij} + (p'-c_0^2\rho_l')\delta_{ij} + c_0^2(1-\alpha_l)(\rho_l-\rho_v)\delta_{ij} \tag{6}$$

where α_l is the volume fraction of fluid and ρ_v is the vapor pressure. As will be explained in the integral formulation presented in Section 2.2, for cavitating flow, the last term in Eq. (6) makes Lighthill stress tensor a combination of monopole and quadrupole source terms.

2.2. Integral formulation of FWH acoustic analogy

The FWH acoustic analogy, i.e. Eq. (1), can be solved by the free space Green's function, and the spatial derivatives can be converted into temporal derivatives. For the surface sound sources, i.e. the first two terms on the right hand side of Eq. (1), this has been done in Farassat (2007). The result is the famous Farassat 1 A formulation,

$$p'_{surf}(\boldsymbol{x},t) = p'_T(\boldsymbol{x},t) + p'_L(\boldsymbol{x},t) \tag{7}$$

where $p'(\boldsymbol{x},t)$ is the sound pressure at the observer $\boldsymbol{x}$ and time t, and the thickness term p'_T and loading term p'_T are

$$4\pi p'_T = \int_{f=0}\left[\frac{\rho_0\left(\dot{U}_n + U_{\dot{n}}\right)}{r\left(1-M_r\right)^2}\right]_{\mathrm{ret}} dS$$

$$+\int_{f=0}\left[\frac{\rho_0 U_n[r\dot{M}_r + c_0\left(M_r - M^2\right)]}{r^2\left(1-M_r\right)^3}\right]_{\text{ret}} dS \tag{8}$$

$$\begin{aligned}4\pi p'_L = &\frac{1}{c_0}\int_{f=0}\left[\frac{\dot{L}_r}{r\left(1-M_r\right)^2}\right]_{\text{ret}} dS\\ &+\int_{f=0}\left[\frac{L_r - L_M}{r^2\left(1-M_r\right)^2}\right]_{\text{ret}} dS\\ &+\frac{1}{c_0}\int_{f=0}\left[\frac{L_r\left\{r\dot{M}_r + c_0\left(M_r - M^2\right)\right\}}{r^2\left(1-M_r\right)^3}\right]_{\text{ret}} dS\end{aligned} \tag{9}$$

where

$$U_i = v_i + \frac{\rho}{\rho_0}\left(u_i - v_i\right) \tag{10}$$

$$L_i = p n_i + \rho u_i(u_n - v_n) \tag{11}$$

In the above equations, f, u, v, ρ, ρ_0, c_0 have the same meaning as in Section 2.1; subscripted variables denote dot products of a vector and a unit vector implied by the subscript, except $L_M = L_i M_i$ whereby M_i presents the vectorial Mach number, i.e. $M_i = v_i/c_0$; r_i is a vector from the source point to observer position, r is its length, and n_i is the unit normal vector on the surface directing into the fluid domain; the dot over a variable means time derivative; the subscript "ret" means that variables inside the square brackets are computed at the corresponding retarded time, i.e. at $\tau = t - r/c_0$.

For the volumetric sound sources, i.e. the third term on the right hand side of Eq. (1), the integral formulation is broadly referenced in literature. The recent work by Nyandeni and Chinyoka (2021) is a good example. The formulation is

$$\begin{aligned}4\pi p'_{vol} = &\frac{1}{c_0^2}\int_{f>0}\left[\frac{\hat{r}_i\hat{r}_j\ddot{T}_{ij}}{r}\right]_{ret} dV\\ &+\frac{1}{c_0}\int_{f>0}\left[\frac{(3\hat{r}_i\hat{r}_j - \delta_{ij})(r\dot{T}_{ij} + T_{ij})}{r^3}\right]_{ret} dV\end{aligned} \tag{12}$$

where $\hat{r}_i$ means the unit vector in the direction of r_i. Here the volume source is stationary, so the Mach number does not appear in the formula.

For specific cavitating cases idealized with Eq. (6), the first integral of Eq. (12) is closely related to the second order time derivative of cavity volume. It contains $\int_{f>0}\left[-\ddot{\alpha}_l(\rho_l - \rho_v)\cdot\frac{\hat{r}_i\hat{r}_j\delta_{ij}}{r}\right]_{ret} dV$, and the volume integration of $-\ddot{\alpha}_l$ is exactly the second order time derivative of cavity volume. This explains theoretically the close relationship between acoustic signal and the second order time derivative of cavity volume, although the multiplier namely $\hat{r}_i\hat{r}_j\delta_{ij}/r$ adds complexity into the relationship. The term $(p' - c_0^2\rho')\delta_{ij}$ in the Lighthill tensor does not contribute to the second integral of Eq. (12), as $(3\hat{r}_i\hat{r}_j - \delta_{ij})\delta_{ij} = 0$.

The strong correlation between acoustic signal and the second time derivatives of cavity volume is also theoretically confirmed by Testa et al. (2018) with FWH acoustic analogy for attached thin sheet cavity on propeller. That was achieved from the loading term p'_T by assuming the blade surface as a fictitious permeable FWH surface and formulating a relative fluid velocity (the transpiration velocity) being the time derivative of cavity thickness on it. The current derivation starts from the volumetric term and has the merit that it poses no limitation on the cavitation form.

Corresponding formulations that account for moving observers are given in Wang et al. (2020) and Brès et al. (2010) for surface sources and in Cianferra et al. (2019) and Najafi-Yazdi et al. (2010) for volumetric sources. In this work moving observers are not considered.

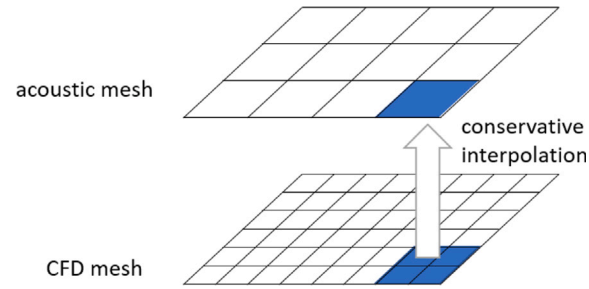

Fig. 1. Interpolation between different meshes.

2.3. Dual mesh technique and numerical implementation

Integrals in Eqs. (8), (9) and (12) are calculated with a first order discretized scheme. Gauss points are located at the center of surface or volume cell. When coupling CFD with the acoustic analogy, one can conduct the acoustic calculations on-the-fly or as part of the post-processing. The latter allows the calculation of acoustic signals at additional observers without running the expensive CFD simulation again. However, it also requires the storage of transient CFD results or at least sound source distributions.

The approach presented in this paper focuses on the volume integration, i.e. Eq. (12). This is because Eq. (12) is the main barrier for the adoption of direct FWH formulation. If we use N_{cell} to denote the number of volume cells where the sound sources are computed or stored, N_{obs} for the number of observers, and N_t for the number of time steps, then the time complexity for acoustic assessment is $O(N_{cell}N_{obs}N_t)$. The disk storage requirement to save data is $O(N_{cell}N_t)$. The time complexity is still acceptable when the number of observers is small. The storage requirement of a single case can, however, easily go up to tens of TB as the CFD simulation tends to using more and more cells. This hinders almost all practical usage of direct FWH formulation.

The idea of the dual mesh technique is to store the sound source information on an acoustic mesh being coarser than the CFD mesh. This technique reduces the computational time and storage requirement by reducing N_{cell}. The sound sources are calculated on-the-fly on CFD mesh and interpolated upon the acoustic mesh, as depicted in Fig. 1. To achieve fast and conservative interpolation, the interpolation is implemented as simple summation (here *conservative* means that the quantities' volume integrals are preserved under re-meshing if the original and target meshes occupy the same space). The acoustic mesh is used to group the CFD cells, i.e. the CFD cells whose center are in the same acoustic cell is grouped together. The CFD and acoustic cells do not need to match in any way. A CFD cell is allowed to fall partially into two different acoustic cells, but it belongs only to one acoustic cell (group) according to its center position. Numerically, the integral of sound source term in each group is calculated as volume weighted summation of the same term in CFD cells, i.e.

$$\Phi_i^{acoustic} = \sum_{j=0}^{N_i}\varphi_{i,j}^{CFD}\cdot V_{i,j}^{CFD} \tag{13}$$

where φ denotes an arbitrary quantity, $\Phi_i^{acoustic} = \left(\int\varphi dV\right)_i^{acoustic}$ denotes its volume integral, i is the index for acoustic cell, N_i is the number of CFD cells associated to the acoustic cell, the subscript (i,j) means jth CFD cell being associated to the ith acoustic cell, and V^{CFD} means the volume of CFD cell. The volume integral Φ is then used directly for acoustic computation. The center of each group is calculated as volume weighted average of the CFD cells center.

To evaluate the volumetric sound sources, the symmetric tensor T_{ij} and group center $x_{c,i}$, i.e. 9 double values for each acoustic cell (or each CFD cell group) are required. The time derivative is calculated with the finite difference method during post processing. When detailed debug

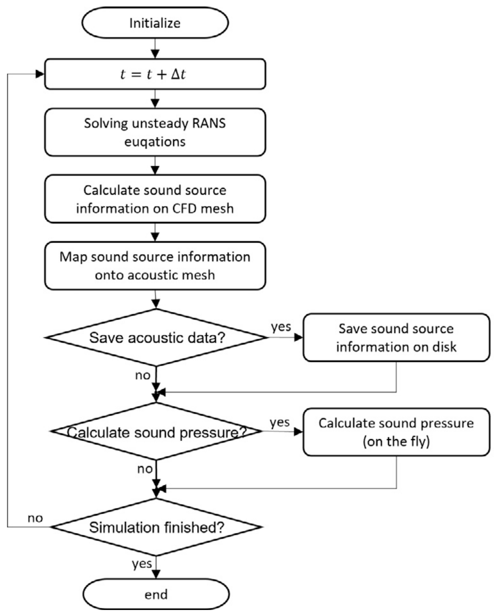

Fig. 2. The flowchart of acoustic calculation during the CFD simulation (Left) and the post processing (Right). The sound pressure is calculated for the time $t+\tau$ and $(t-\Delta t)+\tau$, whereby t and Δt are the CFD time and time step respectively, τ is the sound traveling time from acoustic cell to observer point. Then the sound pressure are interpolated onto an observer time between $t+\tau$ and $(t-\Delta t)+\tau$. The observer time is prescribed with constant time step.

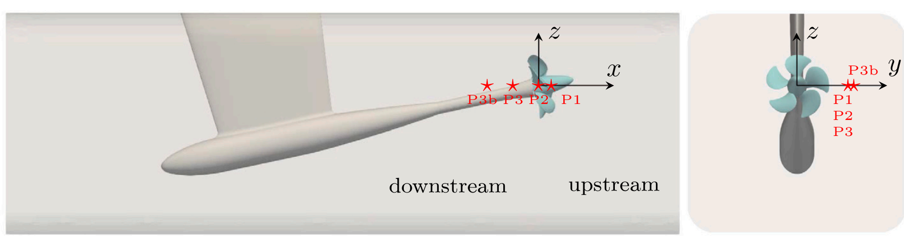

Fig. 3. The PPTC propeller geometry and the measurement arrangement. Left: view from starboard side; Right: view from upstream.

information is needed, the tensors $\rho u_i u_j$, τ_{ij} and scalar $p' - c_0^2\rho'$ are also saved. Then there are totally 22 double values for each acoustic cell.

For the surface sound sources, the information is directly stored on the CFD surface cells. The information includes the scalar U_n, the vectors v_i and L_i, and the cell center $x_{c,i}$. This means 10 double values for each cell.

The dual mesh technique has been implemented together with the FWH acoustic analogy as a library in OpenFOAM, namely *libAcousticsPlus*. The flowchart of the acoustic calculation during the CFD simulation and the post processing is depicted in Fig. 2. The corresponding code has been made open-access under https://gitlab.com/youjiang-wang/libacousticsplus.

3. Numerical result

3.1. Simulation setup

The acoustic analogy must be coupled with CFD for the acoustic assessment. For the verification of the dual mesh technique, the acoustic analogy being implemented is coupled with RANS simulation. The k-Omega SST turbulence model is adopted to close the RANS equation.

The case 2.1 of the SMP'15 propeller workshop (Kinnas et al., 2015) is used as a real-case example to verify the current method. The propeller is the PPTC propeller from SVA, whose diameter is 0.25 m. The propeller was mounted on a shaft being inclined by 12 degrees to have a non-uniform inflow, as shown in Fig. 3. The flow direction is from right to left of the figure, i.e. along the negative x direction. The cavitation tunnel has a section of 0.85 m × 0.85 m. During the experiment, the rotation rate is 20 rps and the advance ratio is 1.019. Other parameters regarding the propeller geometry and measurement are presented in SVA PPTC team (2015).

The sliding mesh technique is used for the simulation. The side view of the overall mesh and the mesh for the rotating domain are shown in Fig. 4. 15 prism layers were generated around the propeller. The average y^+ on the blades are around 60 while the min and max value are 2.5 and 110, respectively. Refined hexagonal mesh were used in the downstream to simulate the tip vortex and slipstream. Totally 9.36M and 2.87M cells are used in the rotating and static domains, respectively.

The simulations were carried out using OpenFOAM v2006. The 2nd order upwind scheme (linear upwind) was used to discretize the convection term. A 2nd order implicit scheme (backward) was used for the temporal discretization. The PIMPLE algorithm was employed to solve the segregated RANS equation, where 15 outer iterations and 2 inner iterations are used. A fixed time step of $2.5{\times}10^{-4}$s, i.e. 1.8 degrees of rotation in each time step, was adopted. The SIMPLEC algorithm was used for the outer iteration of PIMPLE.

To simplify the acoustic calculation, only the volume sources in the rotating domain was considered. As shown in Fig. 5, a uniform Cartesian mesh covers the rotating domain is used as the acoustic mesh. Four observers were located in the very near field beside the propeller, as shown in Fig. 3 and Fig. 6. Their coordinates are (0.05 m, 0.2 m, 0 m) for P1, (0 m, 0.2 m, 0 m) for P2, (−0.1 m, 0.2 m, 0 m) for P3, and (−0.2 m, 0.25 m, 0 m) for P3b. Thus, P1 is 0.2D upstream, P2 is in the propeller disk plane, P3 is 0.4D downstream, and P3b is 0.8D downstream, where D denotes the propeller's diameter. The

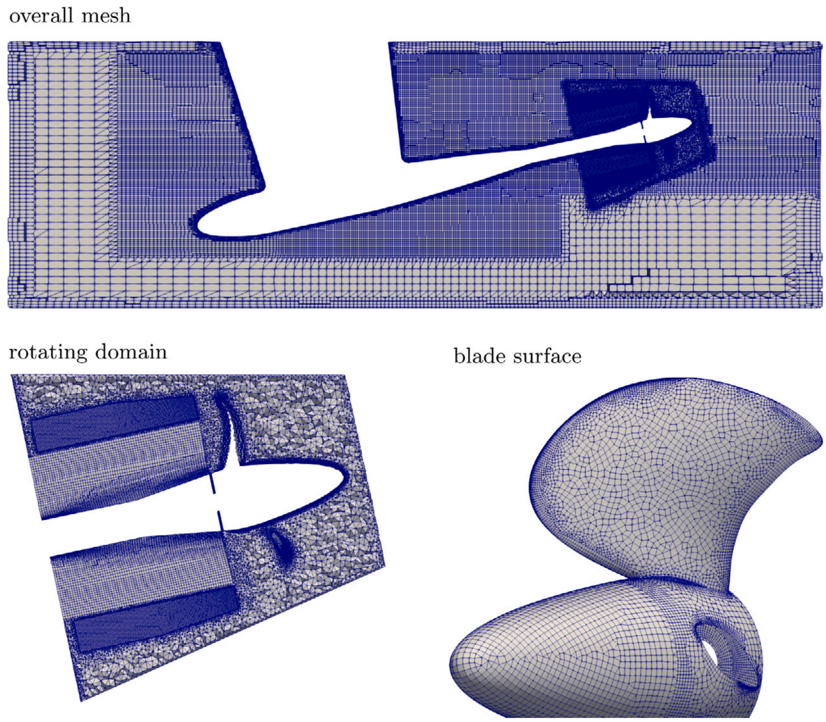

Fig. 4. The CFD mesh used in the simulation.

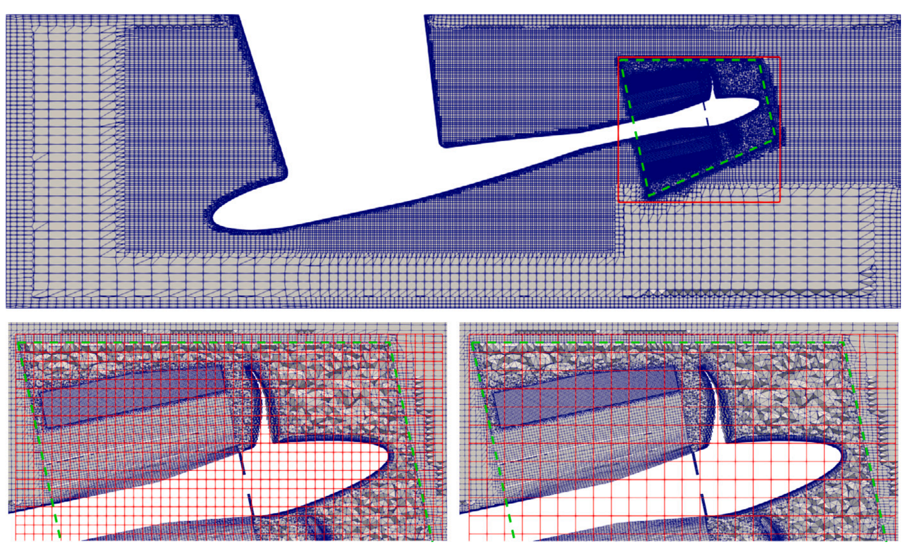

Fig. 5. The relation between CFD mesh (blue) and acoustic mesh (red). The green dashed line denotes the rotating domain. Up: position and outline of the acoustic mesh; Down left: acoustic mesh with cell size being 0.04D; Down right: acoustic mesh with cell size being 0.08D. (For interpretation of the references to color in this figure legend, the reader is referred to the web version of this article.)

reason for the different y coordinate of P3b is to put it outside of the rotating domain, i.e the sound source region. Another ten observers from near field to far field were located in the propeller disk plane on the port side along the positive y axis. Their distances to the propeller center are 0.25 m(P4), 0.5 m(P5), 1 m(P6), 2 m(P7), 4 m(P8), 8 m(P9), 16 m(P10), 32 m(P11), 64 m(P12), and 100 m(P13), respectively.

3.2. Result and Discussion

At first the simulation was ran until the hydrodynamic forces converged to a periodic variation. The variation of thrust and moment along or about the propeller rotation axis are given in Fig. 7. The hydrodynamic forces converged after 0.55 s. The data between 0.52

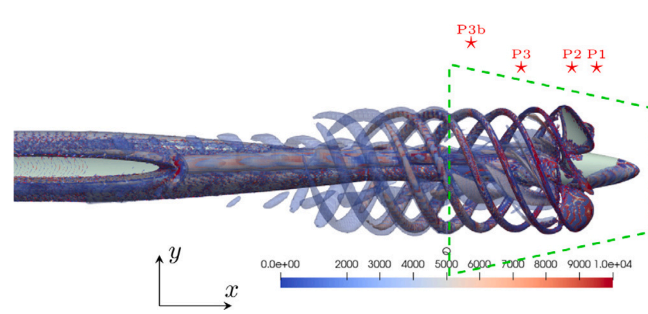

Fig. 6. Positions of observers in the very near field, viewed from upside to downside. The green dashed line represents the outline of rotating domain.

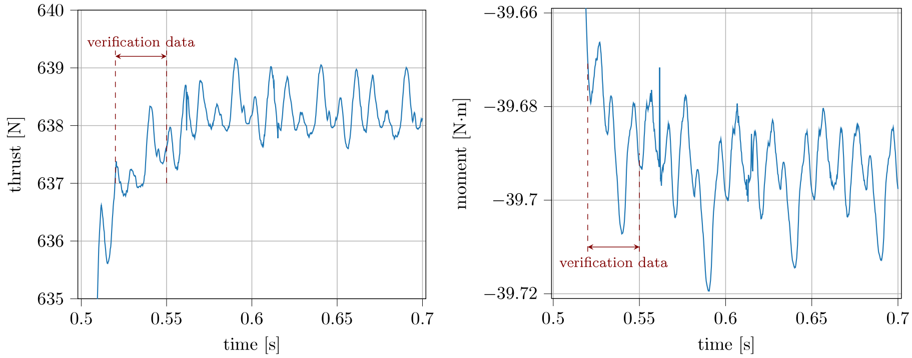

Fig. 7. Variation of propeller thrust along and moment about the propeller rotation axis.

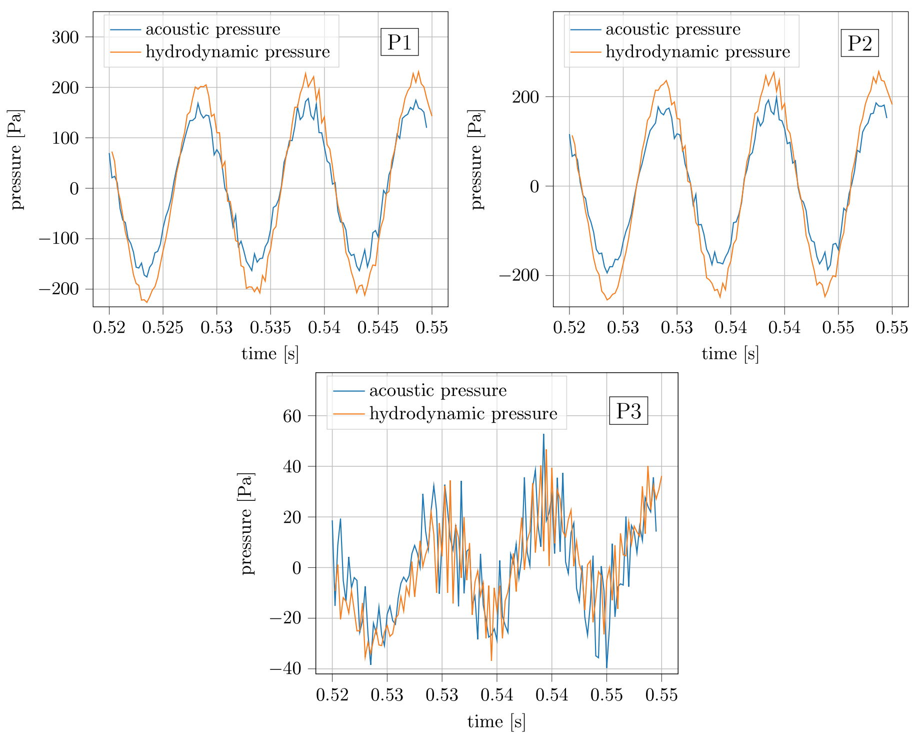

Fig. 8. The comparison between acoustic and hydrodynamic pressures. The pressures have been offset to have a zero mean value. Surface terms on propeller and tunnel walls and volume terms were used for the acoustic evaluation.

and 0.55 s were used for verification of the numerical implementation, and the data between 0.55 and 0.7 s were used for more detail acoustic analysis. The imperfect convergence before 0.55 was found after results were collected. This was caused by numerical treatment when restarting the simulation at 0.5 s. Since the verification was conducted by comparing acoustic results from different calculation methods. Conclusions were not affected by the imperfect convergence.

The acoustic analogy's implementation has been verified by comparing the acoustic and hydrodynamic pressures at three near field positions, i.e. P1, P2, and P3. The pressures were obtained by acoustic calculations and direct probing in the CFD simulation, respectively. The good correlation of results presented in Fig. 8 verifies that the implementation of the FWH acoustic analogy is correct. In this comparison, all boundaries except for the inlet and outlet have been considered in the acoustic calculation. The results show that if the water tunnel walls are ignored, the difference between acoustic and hydrodynamic pressures becomes quite significant. This implies that the sound pressures in the water tunnel are affected significantly by the hydrodynamic pressure fluctuations on the tunnel walls, at least for fully wet cases. Accordingly the affect of tunnel walls as sound sources should be paid attention when conducting acoustic measurement in water tunnels.

To verify the dual mesh technique, the volumetric noise was calculated by using the original CFD mesh and three different acoustic meshes (see Table 1). Acoustic meshes mesh-1 and mesh-2 are also depicted in down left and down right of Fig. 5, respectively. Notably, the acoustic meshes are significantly coarser than the CFD mesh. The disk storage to save the volumetric sound sources and the acoustic calculation time in the post-processing is also given in Table 1. When compared to the CFD mesh, even the finest acoustic mesh (mesh-1) leads to a reduction of storage and calculation time by more than 99% and 98%, respectively.

The sound pressures induced by volumetric sound sources as obtained for various observer positions by different meshes are given in Fig. 9 for various observer positions. The sound pressures obtained with acoustic meshes correlate with those obtained with CFD mesh

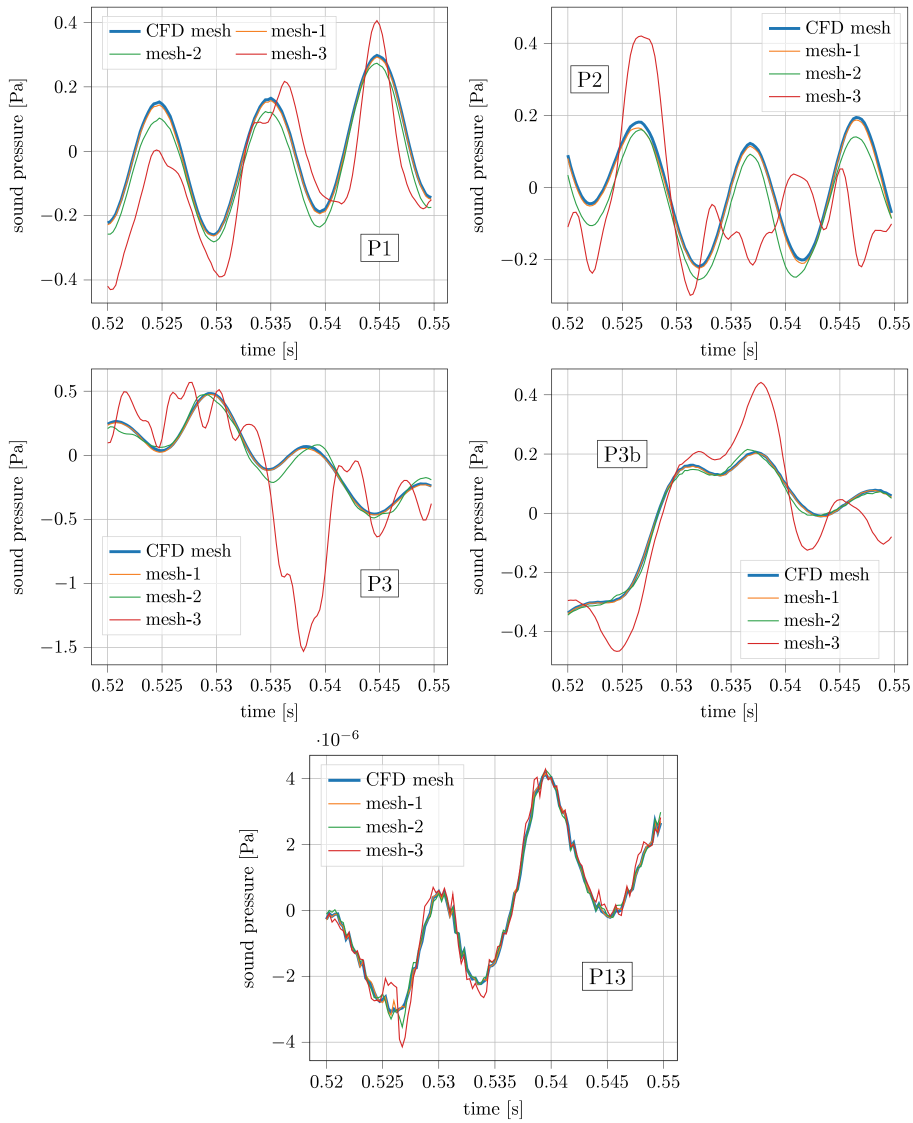

Fig. 9. The comparison between acoustic pressures obtained with different meshes. Only volumetric sound sources were used for computations.

Table 1
The details of acoustic meshes, the disk storage used for volumetric sound sources, and the acoustic calculation time in the post process.

Name	Dimension	Cell size	Disk storage	Acoustic calculation time
CFD mesh			216G	1666 s
acoustic mesh-1	$47 \times 42 \times 42$	0.04D	1.5G	20 s
acoustic mesh-2	$24 \times 21 \times 21$	0.08D	218M	18 s
acoustic mesh-3	$12 \times 10 \times 10$	0.16D	36M	17 s

Table 2
Overall SPL difference between acoustic signals obtained with acoustic mesh and CFD mesh (only volumetric sound sources).

Mesh name	P1	P2	P3	P3b	P13
acoustic mesh-1	0.04 dB	0.19 dB	0.11 dB	0.15 dB	0.01 dB
acoustic mesh-2	0.68 dB	1.82 dB	0.14 dB	0.07 dB	0.10 dB
acoustic mesh-3	2.40 dB	2.52 dB	10.65 dB	4.41 dB	0.51 dB

better at P13 than at P1, P2 or P3, which indicates that the relative differences are smaller in the far field than in the near field. Besides, the discrepancy between results obtained with acoustic and CFD mesh

Table 3
Spectral error between acoustic signals obtained with acoustic mesh and CFD mesh (only volumetric sound sources).

mesh name	P1	P2	P3	P3b	P13
acoustic mesh-1	3.7%	5.6%	3.0%	1.8%	1.1%
acoustic mesh-2	21.8%	34.0%	16.5%	6.5%	3.5%
acoustic mesh-3	52.2%	85.8%	243.9%	74.4%	12.8%

increases as the acoustic mesh becomes coarser. The results obtained with acoustic mesh-1 and CFD mesh almost coincide with each other for all observer positions. A loss of accuracy can be easily observed for mesh-2. Obvious high frequency fluctuation occurs for the coarsest mesh (mesh-3). Mesh-3 is actually not well suited for any acoustic computation.

Frequency domain comparisons are given in Figs. 10 and 11. The energy for frequencies higher than 500 Hz does not appear to decay with increasing frequencies. This is probably caused by numerical errors, e.g. stepwise fluctuations. Again, the differences are smaller in the far field than in the near field. The discrepancy increases as the acoustic mesh becomes coarser. The main acoustic energy is contained in the

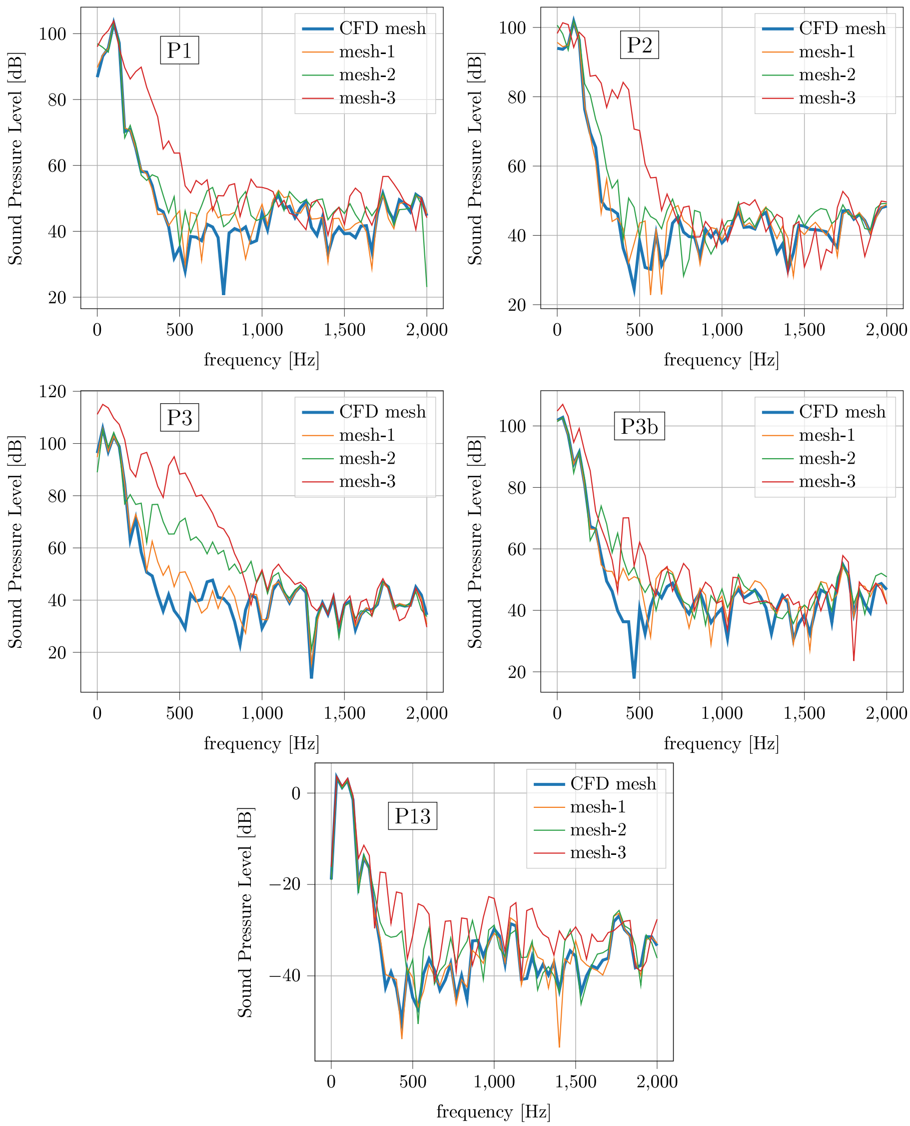

Fig. 10. The comparison between acoustic pressures in the frequency domain obtained with different meshes. Only volumetric sound sources were used for computations.

low frequency, i.e. less than 200 Hz. For this low frequency range, in the near field acoustic mesh-1, mesh-2, and CFD mesh leads to very similar results, while in the far field all acoustic meshes leads to similar results with the CFD mesh. For higher frequency, i.e. around 500 Hz, differences are significant. This is because the acoustic signal obtained with CFD mesh has a trough here. Any tiny temporal difference could move energy to this frequency and leads to a large discrepancy. Even though, the acoustic mesh-1 gives a very good approximation in both near field and far field.

To quantify the error, the overall SPL are compared. Besides, another criterion called spectral error is developed, which is defined as

$$\epsilon_f = \sqrt{\frac{\int \left[p'_1(f) - p'_0(f)\right]^2 \mathrm{d}f}{\int \left[p'_0(f)\right]^2 \mathrm{d}f}} \tag{14}$$

where $p'_0(f)$ is the reference acoustic spectrum and $p'_1(f)$ is the acoustic spectrum to be analyzed. The overall SPL errors are listed in Table 2. The overall SPL differences are small. The maximum difference is less than 2 dB for acoustic mesh-2, and less than 0.2 dB for acoustic mesh-1. The spectral errors are listed in Table 3. One should note that, if two signals are proportional, 12% and 26% spectral errors lead to 1 dB and 2 dB differences, respectively. Thus, we deem that 26% error is acceptable. It can be seen that acoustic mesh-3 error is large in the near field. In contrast to this, in the far field errors of all acoustic meshes are acceptable. The acoustic mesh-1 has a max spectral error of 5.6% for all observers being considered.

A more strict criterion is the max SPL difference in all 1/3 octave bands. This is given in Fig. 12 for acoustic mesh-1 and mesh-2. A general trend is that the error becomes smaller as the distance increases. The max SPL difference between the spectra obtained with acoustic mesh-1 and CFD mesh is less than 10 dB for all distances, and becomes less than 5 dB when the distance goes over 30 m.

Since acoustic mesh-1 can preserve the spectrum well, it was used to investigate the physical property of wet case noise in unsteady flow. In the following, the water tunnel walls are not included in the acoustic calculation. The temporal data in three propeller rotation periods, i.e. from 0.55 to 0.7 s, were used for the acoustic assessment. The analysis considered only frequencies less than 500 Hz. This is because higher frequencies are contaminated by numerical errors and could lead to misleading conclusions. To be noted, in the above verification analysis of dual mesh technique, all frequencies have been considered

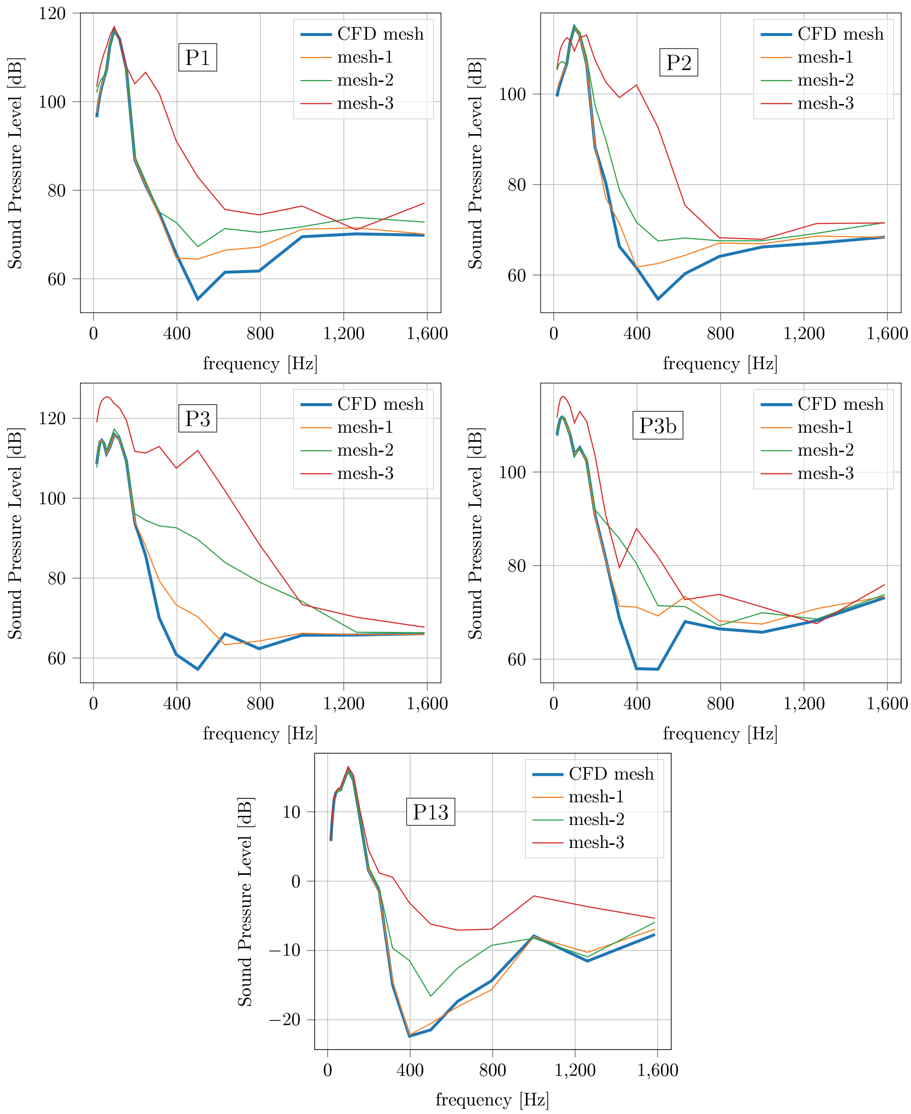

Fig. 11. The comparison between acoustic pressures in 1/3 octave bands obtained with different meshes. Only volumetric sound sources were used for computations.

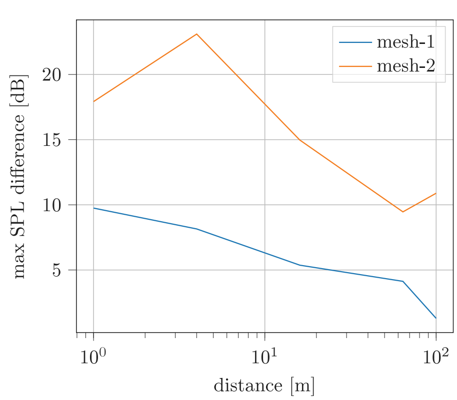

Fig. 12. Max SPL difference in 1/3 octave spectra between results obtained with CFD mesh and acoustic mesh-1 or mesh-2. Only volumetric sound sources were used for computations.

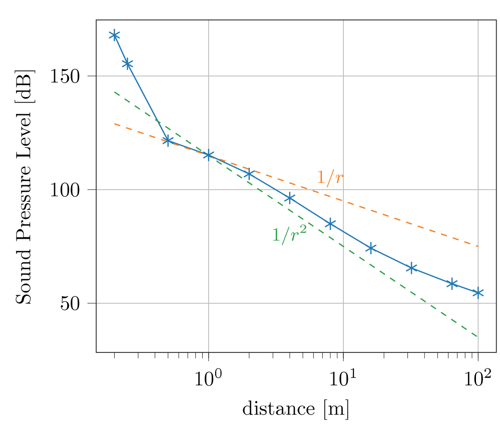

Fig. 13. The decay of overall SPL with distance for the wet case (less than 500 Hz).

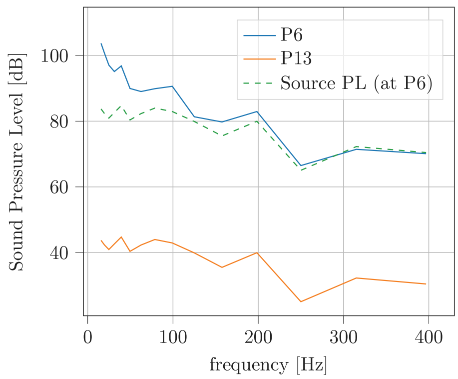

Fig. 14. Spectral comparison of near field and far field noise.

to calculate the results in Table 2, Table 3, and Fig. 12. This is because the above comparisons are pure numerical matters, and the conclusions are not influenced much by the hydrodynamic errors.

The near field and far field were defined on the basis of the noise decay rate. The far field is part of the domain where the sound pressure decays as 1/r. The variation of overall SPL with distance is given in Fig. 13. It can be seen that in the current case, far field corresponds to distances larger than 30 m.

The noise spectra in 1/3 octave bands are compared between a near field position P6 (1 m) and a far field position P13 (100 m), as shown in Fig. 14. In the sea trial measurement, the Source Pressure Level is normally calculated at a distance of 1 m according to the spectra at far field and the 1/r decay rate assumption. The pressure level calculated in this way at P6 is also shown in the same figure. A difference of up to 20 dB between the Source Pressure Level and near field Sound Pressure Level can be easily observed. This could be attributed to the different dominant sound sources in the near field and far field (Wang et al., 2020).

The different components are given in Fig. 15, where $p'_{L,1}$, $p'_{L,2}$, $p'_{L,3}$ are the first, second, and third components in the right hand side of Eq. (9), respectively. It can be observed that in the near field, $p'_{L,2}$ is the dominant sound source, while $p'_{L,1}$ is the dominant sound source in the far field. This is consistent with the findings in Wang et al. (2020). From the formula, we can see that $p'_{L,1}$ decays with $1/r$, while the others with $1/r^2$. Thus, noise measured in the near field may not represent the noise in the far field.

4. Conclusion

This paper presented a novel dual mesh technique that has the potential to reduce the disk storage requirement and calculation time of volumetric sound sources in FWH acoustic analogy. An additional acoustic mesh has been used in the coupling of CFD and acoustic analogy. The volumetric sound sources are calculated on the CFD mesh, but mapped on and saved with the acoustic mesh. The acoustic integration is then conducted on the acoustic mesh. The disk storage and calculation time are reduced in the way that the acoustic mesh has normally much less cells than the CFD mesh. The method has been verified with the inclined PPTC propeller case. In comparison to when CFD mesh is used for acoustic assessment, a reduction of more than 99% disk storage and 98% calculation time for the volumetric noise is achieved, while the sound pressure's temporal variation and spectra are both similar. The difference in overall SPL is less than 0.2 dB and the spectral error is less than 6%. This makes the direct integration of volumetric noise practical for even much refined CFD mesh and helps to avoid the numerical problems with using permeable FWH formulation.

To be clear, the dual mesh technique does not make the direct FWH approach computationally more efficient than the permeable FWH approach, but makes the computational burden increment much less than before. With the dual mesh technique, the direct FWH approach is now also achievable in engineering. One can now choose the direct FWH approach for its merits without worrying too much about the computational resources.

Although we compared three acoustic meshes and observed that the result is satisfactory on the finest mesh, it is too early to conclude the critical acoustic mesh resolution for the dual mesh technique. The critical mesh resolution may depend on the acoustic wave length, position of observers, vortex length scales, etc. Thus, this topic needs more elaborate investigations in the future. A hint from the current work is that the cell size being 0.04 times of the characteristic length scale could be tried with firstly.

A formulation of the Lighthill stress tensor in cavitating flow is also derived. This includes a term being closely related to the cavity volume's second order time derivative. This term includes the local density variation and might show a monopole property in cavitating flow.

In the current investigation, analysis of high frequency noise is hindered by numerical fluctuations. In the future, analysis of the dual mesh technique with more elaborate simulation (with DES or LES) at higher frequencies would be carried out. Besides, application and validation of the dual mesh technique to cavitating situations as well as investigation about critical acoustic mesh resolutions for different scenarios should be conducted.

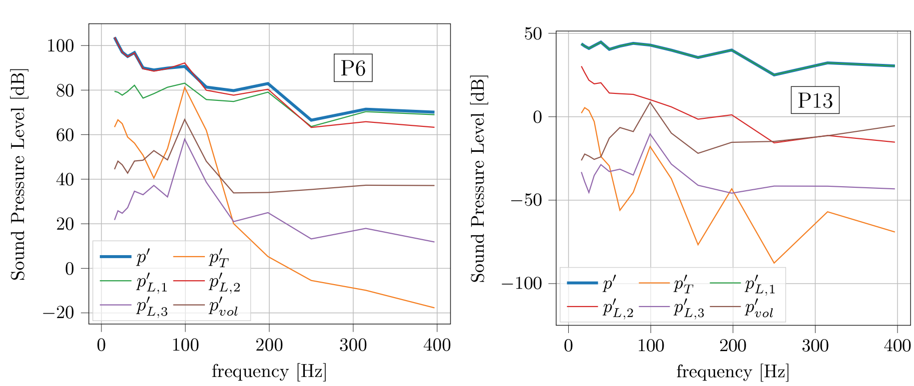

Fig. 15. Spectral comparison of near field and far field noise.

CRediT authorship contribution statement

Youjiang Wang: Conceptualization, Methodology, Software, Validation, Formal analysis, Investigation, Data curation, Writing – original draft, Visualization. **Tommi Mikkola:** Conceptualization, Writing – review & editing, Supervision. **Spyros Hirdaris:** Conceptualization, Writing – review & editing, Supervision, Funding acquisition.

Declaration of competing interest

The authors declare that they have no known competing financial interests or personal relationships that could have appeared to influence the work reported in this paper.

Acknowledgments

This work has been partly supported by the EU Interreg project Green Cruising for Small High Speed Craft (Grant No.: 605111). The first author acknowledges the support of Startup Funding of Shanghai Jiao Tong University (Grant No.: WH220401011). The authors also wish to acknowledge CSC – IT Center for Science, Finland, and the Center for High Performance Computing at Shanghai Jiao Tong University for computational resources.

References

Brès, G.A., Pérot, F., Freed, D., 2010. A ffowcs williams-hawkings solver for lattice-boltzmann based computational aeroacoustics. In: 16th AIAA/CEAS Aeroacoustics Conference (31st AIAA Aeroacoustics Conference).

Cianferra, M., 2017. Acoustic Analogies and Large-Eddy Simulations of Incompressible and Cavitating Flows Around Bluff Bodies (Ph.D. thesis). Università degli Studi di Trieste.

Cianferra, M., Ianniello, S., Armenio, V., 2019. Assessment of methodologies for the solution of the Ffowcs Williams and Hawkings equation using LES of incompressible single-phase flow around a finite-size square cylinder. J. Sound Vib. 453, 1–24.

Curle, N., 1955. The influence of solid boundaries upon aerodynamic sound. Proc. R. Soc. A 231 (1187), 505–514.

Di Francescantonio, P., 1997. A new boundary integral formulation for the prediction of sound radiation. J. Sound Vib. 202 (4), 491–509.

European-Commission, 2019. Our oceans, seas and coasts. URL: https://ec.europa.eu/environment/marine/good-environmental-status/descriptor-11/index_en.htm. (Accessed 31 July 2020).

Farassat, F., 2007. Derivation of Formulations 1 and 1A of Farassat. Technical Report NASA/TM-2007-214853, NASA, Langley Research Center, Hampton, Virginia, USA.

Gadalla, M., Cianferra, M., Tezzele, M., Stabile, G., Mola, A., Rozza, G., 2021. On the comparison of LES data-driven reduced order approaches for hydroacoustic analysis. Comput. & Fluids 216, 104819.

Hirdaris, S., Cheng, F., 2012. The role of technology in green ship design. In: Proceedings of the 11th International Marine Design Conference. IMDC, Glasgow, UK, pp. 11–14.

Hynninen, A., Tanttari, J., Viitanen, V., Sipilä, T., 2017. On predicting the sound from a cavitating marine propeller in a tunnel. In: Proceedings of SMP'17. Espoo, Finland.

Ianniello, S., Muscari, R., Di Mascio, A., 2014. Ship underwater noise assessment by the Acoustic Analogy part II: Hydroacoustic analysis of a ship scaled model. J. Mar. Sci. Technol. 19 (1), 52–74.

Kinnas, S., Abdel-Maksoud, M., Barkmann, U., Lübke, L., Tian, Y., 2015. Proceedings of the Second Workshop on Cavitation and Propeller Performance. Austin, Texas, USA.

Krasilnikov, V., 2019. CFD modeling of hydroacoustic performance of marine propellers: Predicting propeller cavitation. In: Proceedings of the 22nd Numerical Towing Tank Symposium. Tomar, Portugal.

Li, D.-Q., Hallander, J., Johansson, T., 2018. Predicting underwater radiated noise of a full scale ship with model testing and numerical methods. Ocean Eng. 161, 121–135.

Lidtke, A.K., Lloyd, T.P., Vaz, G., 2019. Acoustic modelling of a propeller subject to non-uniform inflow. In: Proceedings of SMP'19.

Lighthill, M.J., 1954. On sound generated aerodynamically II. Turbulence as a source of sound. Proc. R. Soc. A 222 (1148), 1–32.

Lloyd, T.P., Lidtke, A.K., Rijpkema, D., Van Wijngaarden, E., Turnock, S.R., Humphrey, V.F., 2015. Using the FW-h equation for hydroacoustics of propellers. In: 18th Numerical Towing Tank Symposium. NuTTS.

Najafi-Yazdi, A., Brés, G.A., Mongeau, L., 2010. An acoustic analogy formulation for moving sources in uniformly moving media. Proc. R. Soc. Lond. Ser. A Math. Phys. Eng. Sci. 467 (2125), 144–165.

Nyandeni, Z., Chinyoka, T., 2021. Computational aeroacoustic modeling using hybrid Reynolds averaged Navier–Stokes/large-eddy simulations methods with modified acoustic analogies. Internat. J. Numer. Methods Fluids.

Schack, H., Ruiz, M., Andersson, M., Zweifel, U.L., 2019. Noise sensitivity of animals in the Baltic Sea. Helsinki Commission-HELCOM, URL: www.helcom.fi.

Sezen, S., Atlar, M., Fitzsimmons, P., Sasaki, N., Tani, G., Yilmaz, N., Aktas, B., 2020. Numerical cavitation noise prediction of a benchmark research vessel propeller. Ocean Eng. 211, 107549.

Sezen, S., Cosgun, T., Yurtseven, A., Atlar, M., 2021. Numerical investigation of marine propeller underwater radiated noise using acoustic analogy part 2: The influence of eddy viscosity turbulence models. Ocean Eng. 220, 108353.

Spalart, P.R., Belyaev, K.V., Shur, M.L., Kh Strelets, M., Travin, A.K., 2019. On the differences in noise predictions based on solid and permeable surface Ffowcs Williams–Hawkings integral solutions. Int. J. Aeroacoustics 18 (6–7), 621–646.

SVA PPTC team, 2015. Propeller workshop smp'15. URL: https://www.sva-potsdam.de/en/smp15-propeller-workshop. (Accessed 20 December 2021).

Testa, C., Ianniello, S., Salvatore, F., 2018. A Ffowcs Williams and Hawkings formulation for hydroacoustic analysis of propeller sheet cavitation. J. Sound Vib. 413, 421–441.

Testa, C., Porcacchia, F., Zaghi, S., Gennaretti, M., 2021. Study of a FWH-based permeable-surface formulation for propeller hydroacoustics. Ocean Eng. 240 (February), 109828.

Viitanen, V., Hynninen, A., Lübke, L., Klose, R., Tanttari, J., Sipilä, T., Siikonen, T., 2017. CFD And CHA simulation of underwater noise induced by a marine propeller in two-phase flows. In: Proceedings of SMP'17. Espoo, Finland.

Viitanen, V., Hynninen, A., Sipilä, T., Siikonen, T., 2018. DDES of wetted and cavitating marine propeller for CHA underwater noise assessment. J. Mar. Sci. Eng. 6 (2), 56.

Wang, Y., Göttsche, U., Abdel-Maksoud, M., 2020. Sound field properties of non-cavitating marine propellers. J. Mar. Sci. Eng. 8 (11), 885.

Williams, J.F., Hawkings, D.L., 1969. Sound generation by turbulence and surfaces in arbitrary motion. Philos. Trans. R. Soc. Lond. A Math. Phys. Eng. Sci. 264 (1151), 321–342.